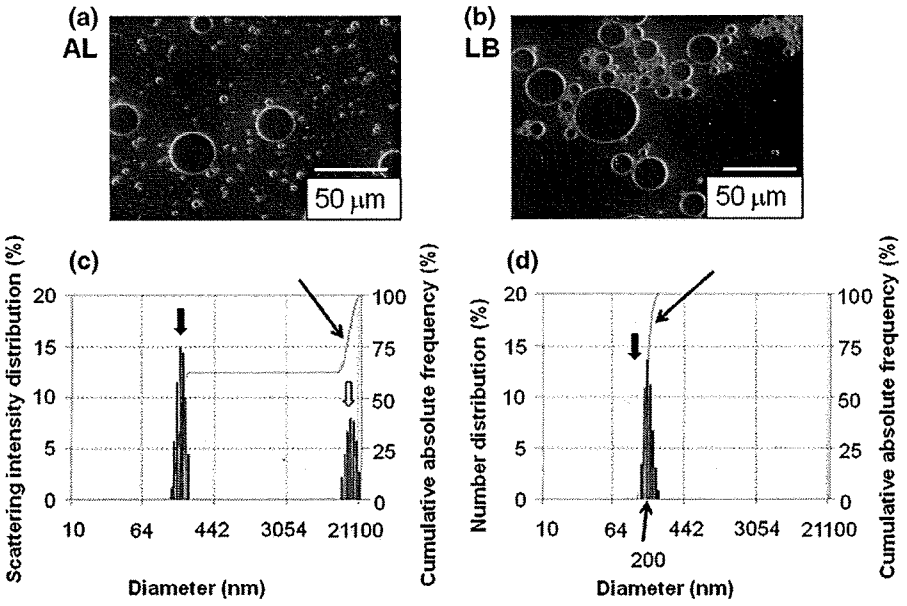

Fig. 1. Dark field images of ALs and LBs and size distribution of ALs. (a) AL dark field image. (b) LB dark field image. (c) Scattering intensity distribution (%) and cumulative absolute frequency (%) of ALs, measured using dynamic light scattering. There are two peaks indicating diameters of ~200 nm (⇓) and 15 700 nm (⇩). (d) Number distribution (%) and cumulative absolute frequency (%) of AL, measured by dynamic light scattering. Approximately 100% of ALs were ~200 nm in diameter (⇓). ALs with diameters exceeding a few micrometers accounted for <0.01%. The arrows (↓) in (c) and (d) indicate the line of the cumulative absolute frequency (%).

2% osmium tetroxide solution, and was fixed at 4°C for 6 h. Dehydration in an ethanol series (50–100%) at room temperature followed, and the solution was embedded in an EPON812 resin mixture at 60°C for 48 h. Thin sections were obtained using an ultramicrotome (Power Tome XL, RMC, Boekeler Instruments, Tucson, AZ, USA). They were stained with 2% uranyl acetate (Merck) for 15 min, washed with rinse solution and were finally stained with a lead stain solution (Sigma, Tokyo, Japan) for 5 min. Histogram of the absolute frequency distribution was obtained from 10 TEM images. The diameter of each AL was measured with rulers.

Brightness analysis

Two sets of TEM images (ALs, and non-gas-containing liposomes [LSs]) were analyzed to assess the average brightness value of the inside of each kind of liposome. The inner area of each liposome on the images was individually selected and its mean brightness value obtained by the ImageJ software (Rasband, W. S., Image J, U. S. NIH, Bethesda, MD, USA, http://rsb.info.nih.gov/ij/, 1997–2009.). For each image, a brightness value of the background was measured and used for normalization. Overstained areas were left out for both types of measurements. Relative brightness values (measured mean brightness/background brightness) were obtained for 106 LSs and 83 ALs.

Statistical analysis

All measurements were represented as either mean ± SD (standard deviation) or SEM (standard error of the mean). Statistical analysis was performed by using Student's *t*-test. Difference with $P < 0.05$ was considered significant. The statistical analysis was performed using Excel 2000 (Microsoft, USA) with the add-in software Statcel 2 [16].

Results

First, the data obtained for ALs and LBs using dark light microscopy were examined, given that both have similar membrane components (Fig. 1a and b). Figure 1a shows that each AL was captured clearly. ALs with a diameter of up to 30 μm existed. Figure 1c shows the percentage of scattering intensity distribution and cumulative absolute frequency of ALs. Two peaks were observed indicating diameters of ~200 nm and 15 700 nm. Figure 1d shows the

Table 1. Bubble characteristics

Nano/microbubble	Shell	Gas	[a]Size (nm)	[b]Zeta potential (mV)
AL	DSPC/DSPE-PEG2000	Perfluoropropane	199 ± 84.4 ($n = 8$)	−2.1 ± 0.9 ($n = 4$)
LB	DSPC/PEG	Perfluoropropane	1222 ± 442.7 ($n = 9$)	−4.2 ± 1.3 ($n = 5$)
AB (Optison)	Albumin	Perfluoropropane	1689 ± 299.8 ($n = 4$)	−40 ± 6.9 ($n = 4$)

[a]Size was measured using dynamic light scattering. Approximately 100% of ALs were ~200 nm in diameter. ALs with diameters larger than a few micrometers accounted for <0.01% (see Fig. 1). Further, 90% of the LBs were ~1200 nm in diameter (data not shown).
[b]The zeta potential was calculated using the Smoluchowski equation.
Values are represented as mean ± SD.

number distribution (%) and cumulative absolute frequency (%), which have been converted from Fig. 1c. Results show that most ALs have diameters of ~200 nm, while ALs with diameters exceeding a few micrometers accounted for <0.01% (Fig. 1c and d). Figure 1b shows the overall LB view. Although large bubbles were visible, the tiny bubbles that were observed in Fig. 1a were not detected in Fig. 1b. The mean diameters for the ALs, LBs and ABs are summarized in Table 1, with AL diameter being one digit smaller than that of the LBs and ABs.

To confirm that the C_3F_8 gas was actually encapsulated by the AL shell, we measured the echogenicity of liposomes sonicated in the presence of either atmospheric air or C_3F_8 gas. Figure 2a shows characteristics of liposomes under either atmospheric air or C_3F_8 gas. Photos show that liposome suspension sonicated in the presence of C_3F_8 is cloudier than that of air and original liposome suspension (NONE). Next we measured echogenicity of each bubble by the method indicated in Fig. 2c. The US B-mode images show that liposome sonicated in the presence of the C_3F_8 gas have a high echogenicity. This tendency is confirmed by the brightness histogram of the liposome sonicated in the presence of the C_3F_8 gas that displays a shift to the right of the brightness levels compared to that with air. Figure 2b indicates the difference of brightness value between liposome sonicated in the presence of either atmospheric air or C_3F_8 gas. The values were normalized by that of NONE. There is a highly significant difference between them ($P < 0.01$).

The zeta potential is one of the primary parameters indicative of drug delivery efficiency, since it informs about dispersivity, aggregability and mutual interaction inside the colloidal suspension. Zeta potential values are summarized in Table 1. ALs and LBs possessed neutral values since neutral lipid phosphatidylcholine was the primary component of their shells and the PEG distributed on their shell surfaces is a nonelectrolyte, water-soluble polymer. ABs had a strong negative charge, indicating that the AB colloid is the most stable of the three bubble types.

Next, ALs were stained using negative staining, and their structures were examined by TEM (Fig. 3). In general, when a lipid bilayer is negatively stained, the stain solution penetrates the lipid bilayer. Existence of gas within certain areas of ALs will prevent that area from being stained effectively, resulting in a reduction in net electron density in that area. The black arrows in Fig. 3a and b indicate the presence of gas within the ALs. Decreased electron density in the central area was apparent in 69 out of 345 ALs, i.e. 20%. The shape of LBs (Fig. 3c and d) was not always spherical as compared to the shapes of ALs. A significant decrease in electron density was not observed in the interior making it difficult to determine whether gas existed in the LB. Figure 3d shows that some LBs had a bag configuration suggesting that an LB may potentially contain both gas and liquid. The AB shell structure caused strong electron beam scattering around the shell (Fig. 3e). As shown in the magnified figure (Fig. 3f), albumin was observed in filament form (indicated by the black arrow), with the layer being several hundred nanometers thick. The interior gas was assumed to be packed in a stable manner and covered with the thick albumin shell. The internal electron density was relatively low, indicating the existence of gas. Figure 4 shows the histogram of the absolute frequency distribution obtained from 10 TEM micrographs. The maximum value was obtained within the class interval of 91–120 nm. This value was about half that measured with dynamic light scattering (see Table 1). Figure 5 shows the distribution of relative brightness values in original liposomes (LSs) and ALs. The statistical distribution of ALs is slightly shifted to relative brightness values closer to 1 compared to the

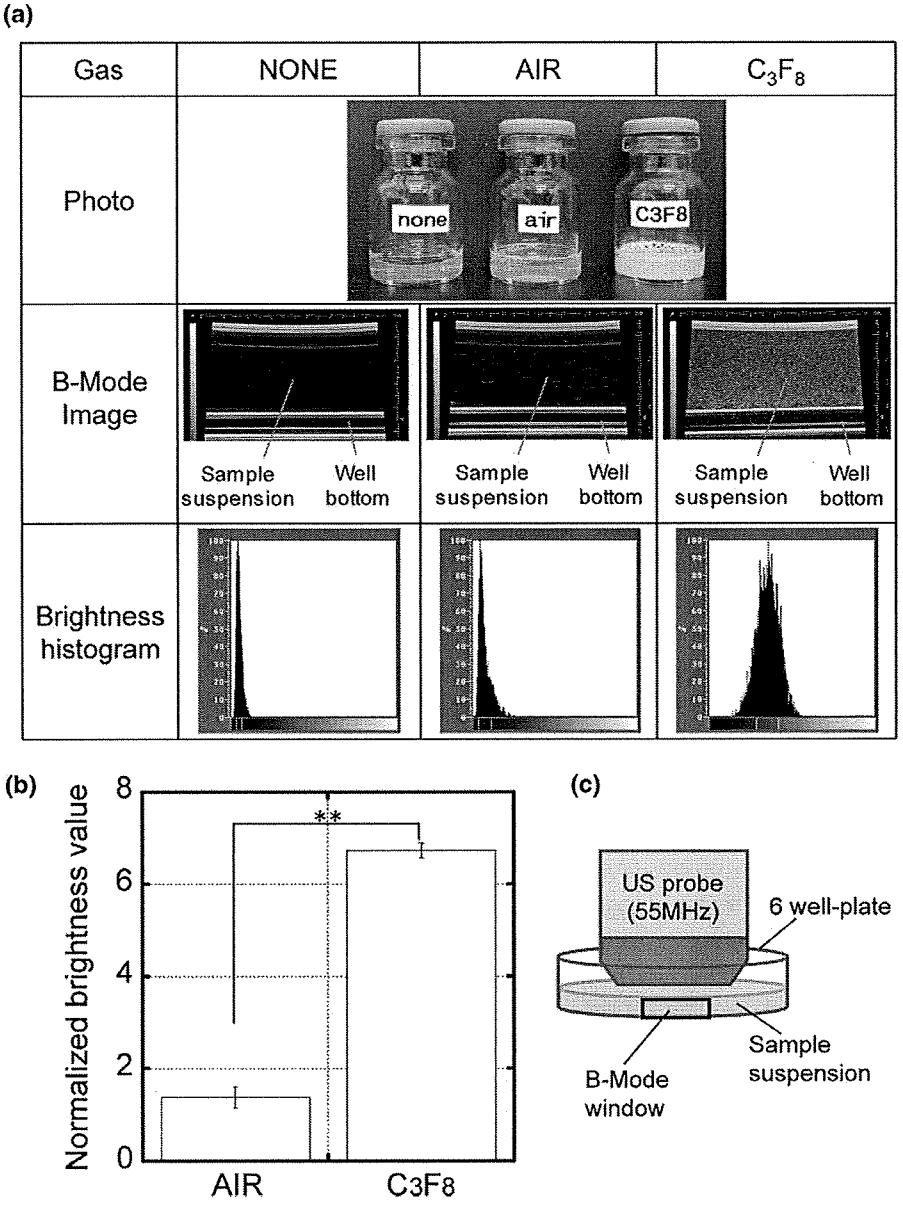

Fig. 2. Confirmation of gas entrapment into liposome. Photos, US B-mode images and brightness histograms of original liposome suspension (none), liposome sonicated under either atmospheric air (air) or C_3F_8 gas (C_3F_8) indicate encapsulation of gas under the presence of the C_3F_8 gas but not in the presence of air (a). The US B-mode images were captured as shown in the scheme for ultrasound imaging (c). There was a highly significant difference in brightness value between liposome sonicated under atmospheric air and C_3F_8 gas. The values were normalized with that of liposome without gas. $n = 4$, mean ± S.E. $^{**}P < 0.01$.

distribution of LSs, indicating that C_3F_8 gas bubbles are actually present inside some of the ALs.

Figure 6 shows a magnified image of the AL, stained at 80°C with the negative staining. The fluidity of lipid layers increases due to heat, and results in the enhanced penetration of the staining solution. The shell thickness was 5.6 nm, which accords with a biomembrane with a thickness of 7–10 nm. Thus, the AL shell is assumed to be a single lipid bilayer.

In order to investigate the AL structure in detail, we observed its cross-section, obtained from the double staining (Fig. 7). The black arrows in Fig. 7a indicate the presence of gas, while the white arrow indicates the presence of liquid. The percentage of

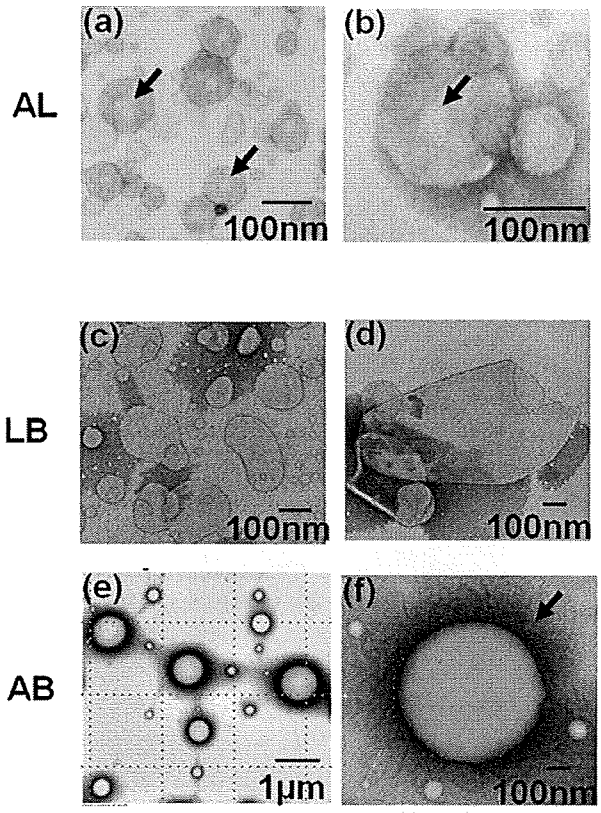

Fig. 3. Three types of ultrasound contrast agent from negative staining. AL: (a) ×50 000, (b) ×100 000. LB: (c) ×15 000, (d) ×10 000. AB: (e) ×3500, (f) ×20 000. The black arrows in (a) and (b) show where electron density was relatively low, indicating the presence of gas. The black arrow in (f) indicates albumin in filament form. (a)–(f) were stained at room temperature. (a), (b) JEOL JEM2000EX operated at 100 kV. (c)–(f) H-7600 operated at 80 kV.

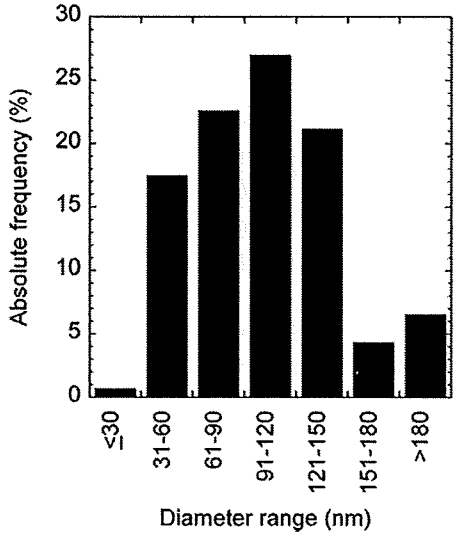

Fig. 4. Histogram of the absolute frequency distribution. The data were obtained from 10 TEM images. The maximum value was obtained within the class interval of 91–120 nm.

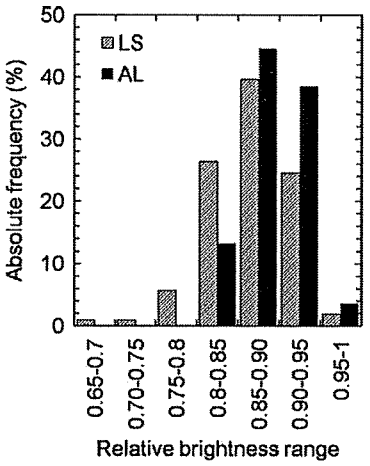

Fig. 5. Relative brightness range. AL and LS TEM micrographs were analyzed to assess the average brightness value of the inside of each kind of liposome. The inner area of each liposome image was digitally selected to measure its mean brightness value. Relative brightness values (measured mean brightness/background brightness) were obtained for 106 LSs and 83 ALs. The statistical distribution of ALs is slightly shifted to relative brightness values closer to 1 compared to the distribution of LSs, indicating that gas bubbles are actually present inside some of the ALs.

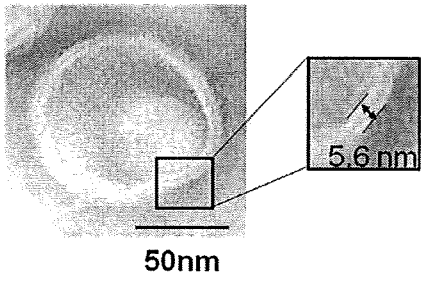

Fig. 6. Shell structure of AL. TEM micrograph of AL, negatively stained at 80°C. The distance between two lines in the magnified figure was 5.6 nm, indicating a single lipid bilayer. Original magnification, ×50 000. JEOL JEM2000EX operated at 100 kV.

AL was 24% (17 out of 70 liposomes). This value was similar to the 20% obtained and illustrated in Fig. 3a and b. Figure 7b shows that some ALs have an equal volume occupied by liquid and gas. The white arrows indicate the outside boundary, while the black arrows indicate the inside boundary. G shows the presence of gas, and L the presence of liquid. It is hard to judge whether the interface between the gas and the liquid within the AL is a gas/liquid interface or a lipid interface. Figure 7c shows an AL primarily occupied by gas. The proportion of gas relative to liquid is likely to vary depending on how the cross-section is cut. Figure 7d shows a liposome which was not sonicated, with a liquid-filled inside.

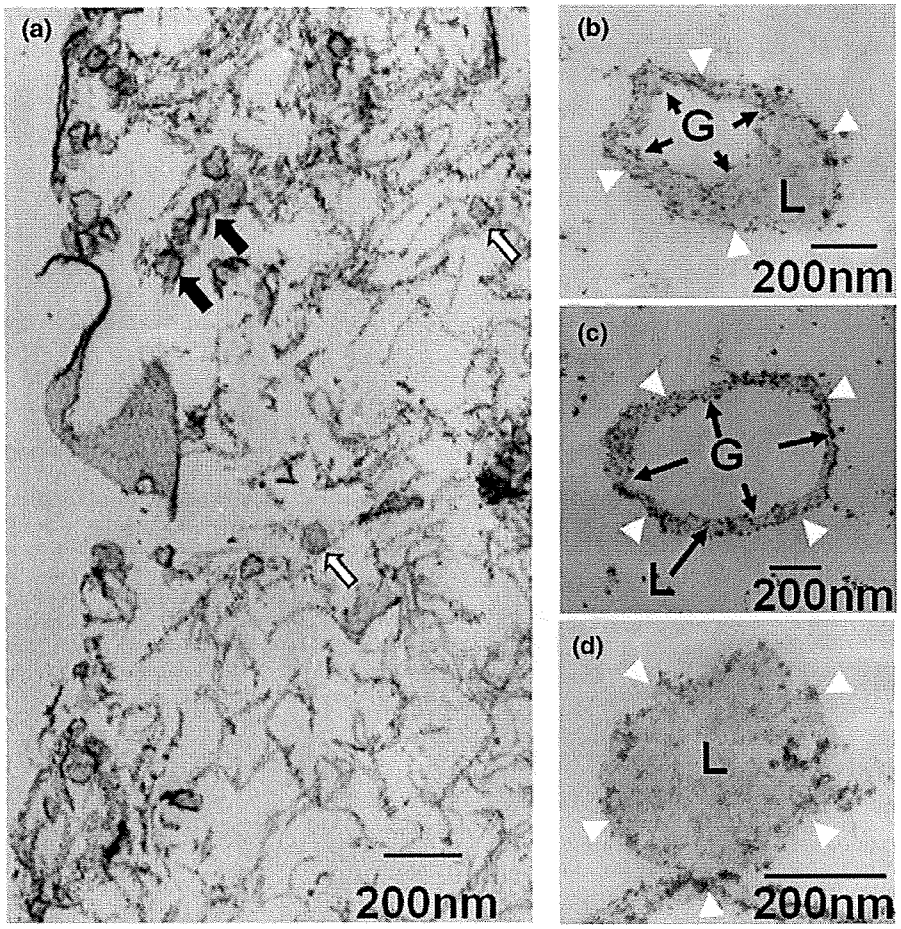

Fig. 7. Structure of AL from double staining. (a) The black arrows indicate the presence of gas in AL, while the white arrow indicates liquid. Original magnification: ×20 000. (b) AL occupied by ~50% (v/v) gas (G) and 50% (v/v) liquid (L). The white arrows indicate the outside boundary, while the black arrows indicate the inside boundary. Original magnification: ×30 000. (c) AL occupied mainly by gas (G). The liquid (L) portion was small. The white arrow indicates the outside boundary, while the black arrow indicates the inside boundary. Original magnification: ×20 000. (d) Liposome, which was not sonicated. The inside was filled with liquid (L). The white arrows indicate the outside boundary. Original magnification: ×50 000. (a)–(d) were obtained with JEOL JEM2000EX operated at 100 kV.

Discussion

The structure of an AL was investigated using TEM, and was compared with that for LB and AB. First we measured the diameter of AL by dynamic light scattering. The diameter of AL was ~200 nm (Table 1), which was about double the diameter calculated from the analysis of 10 TEM micrographs (Fig. 4). With dynamic light scattering, the size was measured immediately after AL production. TEM measurement indicated that the size of AL may have been influenced by the staining process and repeated electron beam exposure. These external factors might shift the frequency distribution to the lower value.

The zeta potential was derived from the hypothesis that ALs, LBs and ABs are hard particles [15]. ALs and LBs were found to be almost neutral, whereas AB had strong negative values (Table 1). As can be seen in TEM images (Fig. 3e and f), the electron beams were strongly scattered around the shell surface of the ABs. The key component of AB, albumin, was detected in its filament form. Ohshima [15] reported that the Smoluchowski equation cannot be applied to soft particles such as red blood cells, i.e. particles with an electric surface charge boundary in which a slip line exists. ABs are most likely to be a type of soft particle, for which this equation cannot be applied. Equations taking into account the properties of this kind of particles should be investigated.

From negative staining observations, it was assumed that AL have a single lipid bilayer as a shell structure (Fig. 6). The percentage of AL in which the presence of gas was detected was ~20%, and the proportion of volume occupied by gas and liquid varied depending on how the cross-sections were cut. Although it was hard to quantify the percentage of gas occupying the interior of AL due to the limited number of TEM images, it was clear from echogenicity that the C_3F_8 gas was actually encapsulated in ALs (Figs. 2 and 5).

Several acoustic liposome structures have been suggested [17,18]. Huang *et al.* [17] proposed that the internal volume was occupied by air and liquid compartments, and that the interface between the air and liquid compartments was a lipid monolayer. Suzuki *et al.* [18] suggested that both liquid and unilamellar lipids containing air were encapsulated by a single lipid bilayer. In the present study, we observed that gas and liquid seemed to be encapsulated together by a single lipid bilayer. However, we could not judge whether the interface between the gas and the liquid was the gas/liquid interface or the lipid interface.

The co-existence of gas and liquid in ALs provides evidence of its echogenicity and drug-carrying capabilities. Further, the tissue specificity of ALs can be improved by conjugating ligands against the target tissue with PEG on the AL surface. Recently, a high-frequency ultrasound system with ALs has been developed and applied so far to the imaging of anterior segment of the eye [19], skin [20] and tumor vasculature [21]. Studies have shown that the permeability of the tumor vasculature is enhanced, and the phenomenon is recognized as the EPR effect [11].

Most anticancer drugs have diameters of 10–120 nm: Genexol-PM (20–50 nm in diameter), Doxil (80–90 nm in diameter), Abraxane (120 nm in diameter) [12]. Sonoporation delivery efficiency, *in vivo* behavior and tissue-specificity of ALs would possibly be enhanced if the diameter was controlled within the range of 10–120 nm, the surface was positively or negatively charged, and ligands against the tumor were conjugated to PEG on the surface [22–24].

Concluding remarks

In summary, the findings of the present study indicate that AL have a shell consisting of a single lipid bilayer and can encapsulate both drugs and gas. The PEG distributed over the surface can be conjugated with tissue-specific ligands. Developing functional AL will assure the effectiveness of sonoporation.

Funding

This work was supported by a Grant-in-Aid for Scientific Research (B) [20300173 to T.K., 19390507 to S.M.]; a Grant-in-Aid for Scientific Research on Priority Area, MEXT [20015005 to T.K.]; a Grant for Research on Advanced Medical Technology, the Ministry of Health, Labor and Welfare of Japan [H19-nano-010 to T.K.]; a Grant for Research on Development of Systems and Technology for Advanced Measurement and Analysis, JST [T.K.]; and a Grant-in-Aid for JSPS Fellows [21-7271 to S.H.].

Acknowledgements

The authors would like to thank Yukiko Watanabe, Rui Chen and Li Li, for their technical assistance.

References

1 Kodama T, Tomita Y, Koshiyama K, and Blomley M J (2006) Transfection effect of microbubbles on cells in superposed ultrasound waves and behavior of cavitation bubble. *Ultrasound Med. Biol.* **32**: 905–914.

2 Lindner J R (2004) Microbubbles in medical imaging: current applications and future directions. *Nat. Rev. Drug Discov.* **3**: 527–532.

3 Shohet R V, Chen S, Zhou Y T, Wang Z, Meidell R S, Unger R H, and Grayburn P A (2000) Echocardiographic destruction of albumin microbubbles directs gene delivery to the myocardium. *Circulation* **101**: 2554–2556.

4 Christiansen J P, French B A, Klibanov A L, Kaul S, and Lindner J R (2003) Targeted tissue transfection with ultrasound destruction of plasmid-bearing cationic microbubbles. *Ultrasound Med. Biol.* **29**: 1759–1767.

5 Suzuki R, Takizawa T, Negishi Y, Utoguchi N, Sawamura K, Tanaka K, Namai E, Oda Y, Matsumura Y, and Maruyama K (2008) Tumor specific ultrasound enhanced gene transfer *in vivo* with novel liposomal bubbles. *J. Control. Release* **125**: 137–144.

6 Suzuki R, Oda Y, Utoguchi N, Namai E, Taira Y, Okada N, Kadowaki N, Kodama T, Tachibana K, and Maruyama K (2009) A novel strategy utilizing ultrasound for antigen delivery in dendritic cell-based cancer immunotherapy. *J. Control. Release* **133**: 198–205.

7 Church C C (1995) The effrcts of an elastic solid-surface layer on the radial pulsations of gas-bubbles. *J. Acoust. Soc. Am.* **97**: 1510–1521.

8 Kodama T, Tomita Y, Watanabe Y, Koshiyama K, Yano T, and Fujikawa S (2009) Cavitation bubbles mediated molecular delivery during sonoporation. *J. Biomech. Sci. Eng.* **4**: 124–140.

9 Suzuki R, Takizawa T, Negishi Y, Hagisawa K, Tanaka K, Sawamura K, Utoguchi N, Nishioka T, and Maruyama K (2007) Gene delivery by combination of novel liposomal bubbles with perfluoropropane and ultrasound. *J. Control. Release* **117**: 130–136.

10 Klibanov A L, Maruyama K, Torchilin V P, and Huang L (1990) Amphipathic polyethyleneglycols effectively prolong the circulation time of liposomes. *FEBS Lett.* **268**: 235–237.

11 Matsumura Y and Maeda H (1986) A new concept for macromolecular therapeutics in cancer chemotherapy: mechanism of tumoritropic

accumulation of proteins and the antitumor agent smancs. *Cancer Res.* **46**: 6387–6392.

12 Davis M E, Chen Z G, and Shin D M (2008) Nanoparticle therapeutics: an emerging treatment modality for cancer. *Nat. Rev. Drug Discov.* **7**: 771–782.

13 Aoi A, Watanabe Y, Mori S, Takahashi M, Vassaux G, and Kodama T (2008) Herpes simplex virus thymidine kinase-mediated suicide gene therapy using nano/microbubbles and ultrasound. *Ultrasound Med. Biol.* **34**: 425–434.

14 Watanabe Y, Aoi A, Horie S, Tomita N, Mori S, Morikawa H, Matsumura Y, Vassaux G, and Kodama T (2008) Low-intensity ultrasound and microbubbles enhance the antitumor effect of cisplatin. *Cancer Sci.* **99**: 2525–2531.

15 Ohshima H (1994) Eectrophoretic mobility of soft particles. *J. Colloid Interface Sci.* **163**: 474–483.

16 Yanai H (2007) *Statcel—The Useful Add-in Forms on Excel.* (OMS, Tokyo).

17 Huang S L, and Macdonald R C (2004) Acoustically active liposomes for drug encapsulation and ultrasound-triggered release. *Biochim. Biophys. Acta* **1665**: 134–141.

18 Suzuki R, Takizawa T, Negishi Y, Utoguchi N, and Maruyama K (2008) Effective gene delivery with novel liposomal bubbles and ultrasonic destruction technology. *Int. J. Pharm.* **354**: 49–55.

19 Pavlin C J, and Foster F S (1998) Ultrasound biomicroscopy. High-frequency ultrasound imaging of the eye at microscopic resolution. *Radiol. Clin. North Am.* **36**: 1047–1058.

20 Vogt M, and Ermert H (2008) Limited-angle spatial compound imaging of skin with high-frequency ultrasound (20 MHz). *IEEE Trans. Ultrason. Ferroelectr. Freq Control* **55**: 1975–1983.

21 Lyshchik A, Fleischer A C, Huamani J, Hallahan D E, Brissova M, and Gore J C (2007) Molecular imaging of vascular endothelial growth factor receptor 2 expression using targeted contrast-enhanced high-frequency ultrasonography. *J. Ultrasound Med.* **26**, 1575–1586.

22 Schneider M (2008) Molecular imaging and ultrasound-assisted drug delivery. *J. Endourol.* **22**: 795–802.

23 Kaufmann B A, and Lindner J R (2007) Molecular imaging with targeted contrast ultrasound. *Curr. Opin. Biotechnol.* **18**: 11–16.

24 Palmowski M, Huppert J, Hauff P, Reinhardt M, Schreiner K, Socher M A, Hallscheidt P, Kauffmann G W, Semmler W, and Kiessling F (2008) Vessel fractions in tumor xenografts depicted by flow- or contrast-sensitive three-dimensional high-frequency Doppler ultrasound respond differently to antiangiogenic treatment. *Cancer Res.* **68**: 7042–7049.

Journal of Biomechanical Science and Engineering

Vol. 4, No. 1, 2009

Cavitation Bubbles Mediated Molecular Delivery During Sonoporation*

Tetsuya KODAMA**, Yukio TOMITA***, Yukiko WATANABE**, Kenichiro KOSHIYAMA****, Takeru YANO***** and Shigeo FUJIKAWA******

**Graduate School of Biomedical Engineering, Tohoku University, Japan,
2-1 Seiryo, Aoba, Sendai 980-8575, Japan
E-mail: kodama@bme.tohoku.ac.jp
***Faculty of Education, Hokkaido University of Education, Japan,
****Graduate School of Engineering Science, Osaka University, Japan,
*****Graduate School of Engineering, Osaka University, Japan,
******Graduate School of Engineering, Hokkaido University, Japan

Abstract

Molecular delivery using ultrasound (US) and nano/microbubbles (NBs), i.e., sonoporation, has applications in gene therapy and anticancer drug delivery. When NBs are destructed by ultrasound, the surrounding cells are exposed to mechanical impulsive forces generated by collapse of either the NBs or the cavitation bubbles created by the collapse of NBs. In the present study, experimental, theoretical and numerical analyses were performed to investigate cavitation bubbles mediated molecular delivery during sonoporation. Experimental observation using lipid NBs indicated that increasing US pressure increased uptake of fluorescent molecules, calcein (molecular weight: 622), into 293T human, and decreased survival fraction. Confocal microscopy revealed that calcein molecules were uniformly distributed throughout the some treated cells. Next, the cavitation bubble behavior was analyzed theoretically based on a spherical gas bubble dynamics. The impulse of the shock wave (i.e., the pressure integrated over time) generated by the collapse of a cavitation bubble was a dominant factor for exogenous molecules to enter into the cell membrane rather than bubble expansion. Molecular dynamics simulation revealed that the number of exogenous molecules delivered into the cell membrane increased with increasing the shock wave impulse. We concluded that the impulse of the shock wave generated by cavitation bubbles was one of important parameters for causing exogenous molecular uptake into living cells during sonoporation.

Key words: Nanoparticles, Membrane Permeabilization, DDS, Fluorescence

1. Introduction

Nano/microbubbles (NBs) are encapsulated gas bubbles with a radius between 50 nm and 5 μm. These bubbles oscillate nonlinearly in an ultrasound (US) field and emit acoustic signals with harmonic and subharmonic components, on the basis of which their acoustic scattering and vasculature signatures are distinguished [1]. The shell membrane of NBs is composed of albumin, lipid, or polymer. The gas inside the bubble is either air or perfluorocarbons. Large molecules such as C_3F_8 prolong enhancement time because of decreased diffusion [2][3]. Ligands that are able to bind disease-related markers can be incorporated on the surface of the bubbles; thus, the bubbles can have an active function to move toward the target sites [4]. Several engineered bubbles that are aimed at targeting inflammation, angiogenesis, early tumor formation, and thrombi have been reported in the

*Received 22 July, 2008 (No. 08-0493)
[DOI: 10.1299/jbse.4.124]

literature [5].

NBs have been used to modulate targeted molecular mediators. Conceptually, NBs are mixed with exogenous molecules such as therapeutic genes or anticancer drugs and injected either locally or systemically. Targeted gene transfer is then achieved by destructing NBs located in a selective defined area [6][7][8]. The mechanical index (*MI*) for destructing NBs is reported to be 0.1 - 0.5 [9][10][11][12], where *MI* is defined as the peak negative pressure divided by the square root of the US frequency. The efficiency of molecular delivery depends on the US parameters (exposure time, intensity, pulse length, and duty cycle of US) [13][14], the membrane components of the NBs [15][16], and the cell-to-NB ratio [17][18].

Collapse of NBs generates second products such as many tiny bubbles as well as debris that have gas attached or included as modeled by Harvey *et al.*[19]. Since NBs and the second products behave as cavitation nuclei [20][21][22], cavitation bubbles generate from them in a field of US. Broadband noise measurements detected the generation of cavitation bubbles in the presence of US with varying pressures from 0.5 to 2.0 MPa [23].

NBs and cavitation bubbles generate mechanical forces such as bubble expansion, microstreaming, liquid jet impact, and shock waves. These forces interact with the surrounding cells, resulting in transient membrane permeability, followed by the entry of exogenous molecules [24][25][26].

The pressure profile of a shock wave indicates its energy content, and shock-wave propagation in tissue is associated with cellular displacement, leading to the development of cell deformation. The efficiency of molecular delivery depends on the molecular size of exogenous molecules [27][28], and the application time of shock waves [28][29]. Kodama et al. [30] reported that the impulse of the shock wave (i.e., the pressure integrated over time) was a dominant factor for membrane permeability. Molecular dynamics (MD) simulation has shown that shock wave impulse induces water molecule penetration [31][32] and formation of transient water pores in a lipid bilayer [33].

In the present study, experimental, theoretical and numerical analyses were performed to investigate cavitation bubbles mediated molecular delivery during sonoporation. The impulse of the shock wave generated by cavitation bubbles was shown as one of important parameters for causing exogenous molecular uptake into living cells in sonoporation.

2. Materials & Methods

2.1. Experiment

Ultrasound

US was generated at 1.0 MHz by using a 12-mm-diameter submersible piezoceramic transducer (Fuji Ceramics Co., Tokyo, Japan) in a test chamber (300 × 450 × 300 mm, L × W × H) filled with tap water. A 1.0-MHz sine wave (sinusoid) was generated using a multifunction synthesizer (WF1946A; NF Co., Yokohama, Japan) and amplified with a high-speed bipolar amplifier (HSA4101; NF Co.). The pressure values were measured using a PVDF needle hydrophone (PVDF-Z44-1000; Specialty Engineering Associates, Soquel, CA, USA) at a standoff distance of 1 mm from the transducer surface. The signals from the hydrophone were amplified and recorded into a digital oscilloscope (500 MHz, 1 MΩ (16 pF), Wave Surfer 454; LeCroy Co., Chestnut, NY, USA). The peak positive acoustic pressures were 0.2, 0.3, and 0.5 MPa, and each pressure corresponded to the calculated acoustic intensity of 1.3, 3.0, and 8.3 W/cm^2, respectively. The intensity was defined as the average rate of energy flow through a unit area normal to the direction of propagation. *MI* was 0.2, 0.3, and 0.5, respectively. The values of the peak positive pressures were the same as those of the peak negative pressures. The duty ratio was 50%; number of pulses, 2000;

pulse repletion frequency (PRF), 250 Hz; and exposure time, 10 s.

Nano/microbubbles

Lipid NBs were created in an aqueous dispersion of 2 mg/mL 1,2-distearoyl-*sn*-glycero-3-phosphocholine (Avanti Polar Lipids, Alabaster, AL, USA) and 1 mg/mL polyethylene glycol 40 stearate (Sigma-Aldrich Co., St. Louis, MO, USA) by using a 20-kHz sonicator (Vibra Cell™; Sonics & Materials, Inc., Danbury, CT, USA) in the presence of C_3F_8 gas. The presence of lipid molecules in the lipid NB surface was confirmed by staining with 3 μM FM1-43 (excitation: 553 nm, emission: 570 nm; Molecular Probe Inc., Eugene, OR, USA) and observation under an inverted microscope (IX81; Olympus Co., Tokyo, Japan). The mean concentration was 3.4×10^8 bubbles/mL. The peak diameters expressed in terms of size distribution and zeta potential were 1272 ± 163 nm (n = 7, mean ± S.D.) and –4.11 ± 0.74 mV (n = 4, mean ± S.D.), respectively (Fig. 1). Both values were measured by using a laser diffraction particle size analyzer (particle range of 0.6 nm –7 μm, ELSZ-2; Otsuka Electronics Co. Ltd, Osaka, Japan) in phosphate-buffered saline without Mg^{2+} and Ca^{2+} (PBS, pH 7.2 at room temperature, Sigma-Aldrich) [34].

Cell culture

In vitro studies were performed in accordance with the ethical guidelines of Tohoku University. Human embryonic kidney (293T) cells were obtained from Prof. M. Ono (Tohoku University, Japan) and were cultured in Dulbecco's modified Eagle's medium (DMEM) containing 10% fetal bovine serum and 1% penicillin-streptomycin in 250 mL culture flasks in a cell culture incubator (SCI-325D; Astec Co., Fukuoka, Japan) at 37°C under an atmosphere of 5% CO_2 in air. Prior to the US-mediated delivery experiments, the total cell counts and viability were determined using a hemocytometer with the trypan blue dye exclusion method [35]. Only cells that were in the exponential growth phase and had a viability of ≥ 99% were used.

Fluorophores

Calcein (622 Da) (excitation: 496 nm, emission: 514 nm; Sigma-Aldrich Co.) was used for the evaluation of the uptake of molecules by the cells in the presence of US and NBs. Calcein was dissolved in PBS and used at a concentration of 200 μM in a complete medium. Stokes radius for calcein was estimated to be 0.68 nm [30].

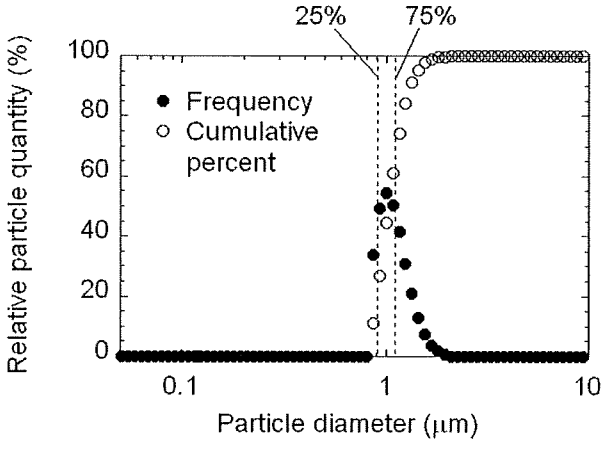

Fig. 1 Size distribution of lipid NBs. The mean peak of size distribution was 1.27 ± 0.431 μm (n = 7, mean ± S. D.). ○: cumulative percent, ●: frequency, n: number of samples.

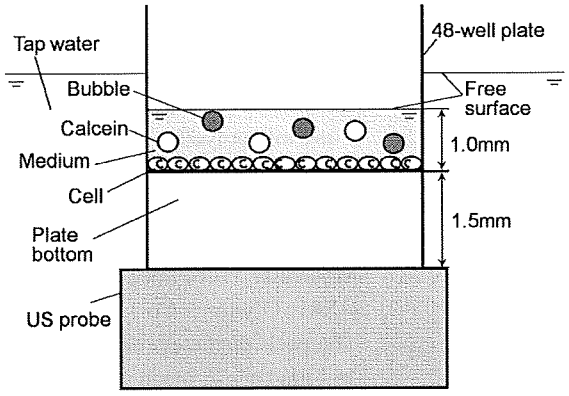

Fig. 2 Experimental setup. The 48-well culture plates were positioned just above the 1-MHz US probe in a test chamber (300 × 450 × 300 mm, L × W × H) filled with water. The basal plate thickness of the 48-well culture plate was 1.5 mm. By assuming the speed of sound in water to be 1500 m/s, we calculated the wavelength as 1.5 mm. The height of the medium containing calcein and lipid NBs in the plate was 1 mm. Complexed superimposed ultrasonic waves were generated in the medium. Atomized particles were generated with increasing US intensity, indicating the generation of cavitation bubbles.

Ultrasound exposure

Cells were seeded onto 48-well plates alternately at 5×10^4 cells/well in a complete medium and incubated at 37°C in a 5% CO_2 incubator. After a 24-h attachment period, the seeded cells were washed with PBS, and the medium was replaced with a fresh medium (110 μL) containing calcein (200 μM) with and without NBs (10% v/v). The height of the medium containing calcein and lipid-micelle bubbles in the plate was 1 mm. The maximum geometrical characteristic radius r_0 occupied uniformly by a single NB (eqn (A2)) for a lipid bubble was calculated to be 19 μm. The US transducer was placed in the test chamber filled with tap water, and the plates were positioned just above the US probe (Fig. 2). The basal plate thickness of the 48-well culture plate was 1.5 mm. When the speed of sound in water was assumed to be 1500 m/s, the wavelength was calculated to be 1.5 mm. Superimposed ultrasonic waves were generated in the media, and atomized particles were generated with increasing US intensity. The generation of particles indicated the generation of cavitation bubbles, as mentioned in the Results and Discussion section. The cells were exposed to US with a pressure of 0.2, 0.3, and 0.5 MPa at a duty ratio of 50% for 10 s. The number of cycles in the pulse was 2000. Twenty-four wells of the 48-well plate were used for each condition. Since the cells were seeded onto alternate wells, the neighboring wells were not exposed to US at the same time. Cell viability was determined using the MTT (3-[4,5-dimethylthiazol-2-yl]-2,5-diphenyltetrazolium bromide) assay as described previously [36], and the cell survival fractions were expressed relative to cells not treated with NBs and US (control).

Fluorescence measurement

After the US exposure, supernatants from 6 wells of the 48-well plate were collected in a 15-mL centrifuge tube. The cells in the wells were washed with 500 μL PBS, and the PBS containing the cells was transferred to the abovementioned centrifuge tubes. All the cells were trypsinized (100 μL/well) and transferred to each centrifuge tube. The cells were washed with PBS (14 mL, 3×) to remove the excess extracellular fluorophore by centrifugation (5 min at 350 × *g*). Then, 1 mL PBS was added to the centrifuge tubes, and the cells were transferred to an eppendorf tube and centrifuged at 8000 × *g* for 5 min. After the supernatant was discarded, the pellet was lyzed with 200 μL of reporter lysis buffer

(Promega, Madison, WI, USA) and subsequently frozen at –80°C for 15 min. The cells were defrosted on ice. Each lysate was centrifuged at 12000 × *g* for 2 min to pellet cell debris. Twenty microliters of the lysate was analyzed for the uptake of fluorescent molecules by using an Mx3000P™ (Stratagene, La Jolla, CA, USA). The fluorescence was excited using a quartz tungsten halogen lamp (350–750 nm), and the emission was collected through a band-pass filter of 492–516 nm. The fluorescence data was analyzed with MxPro™ QPCR Software (Stratagene). The total protein content in an aliquot of each sample supernatant was calculated with albumin standard curves (BCA protein assay kit; Pierce, Rockford, IL, USA). Two additional standard curves were utilized; one for the cell number and its total protein content, and the other for fluorescence concentration and its fluorescence intensity. Duplicates of the samples and standards were used for the experiment, and the absorption of the protein was measured at 562 nm by using a plate reader (Sunrise; Tecan Austria GmbH, Salzburg, Austria) with the data analysis software LS-PLATEmanager RD (Windows) 2001 (Sunrise). The number of equivalent fluorescent molecules per cell was determined from the calibration curves.

Confocal fluorescence microscopy

293T cells (5×10^4 cells/well) were seeded in a complete medium in alternate 48 wells to prevent the exposure of neighboring cells to US. The medium was replaced on the next day with a fresh medium (110 μL) containing calcein (200 μM) with and without NBs (10% v/v). After an US exposure of 10 s, the plates were incubated for 24 h. The cells were then washed 3 times with PBS and trypsinized. Finally, the cell pellet was resuspended in 60 μL of 0.7 μg/mL propidium iodide (PI, excitation: 535 nm, emission: 617 nm, Molecular Probes) and incubated at room temperature for 10-15 min. Confocal fluorescence microscopy was performed using a confocal microscope (FV1000, Olympus). A 60× oil-immersion objective lens with a numerical aperture of 1.25 was used. Calcein and PI fluorescence was excited with a 488-nm line of an argon laser. The laser excitation beam was directed to the specimen through a 488-nm dichroic beam splitter. Emitted fluorescence was collected through a 510- to 550-nm band-pass emission filter for the green channel and a 580-nm long-pass filter for the red channel. Computer-generated images of 1-μm optical sections were obtained at the approximate geometric center of the cell as determined by repeated optical sectioning.

Statistical analysis

All the measurement values are expressed as either mean ± S.D. (standard deviation) or mean ± S.E.M. (standard error of means). Statistical analysis for the calcein uptake was performed by Kruskal-Wallis test. When the Kruskal-Wallis test was significant, the differences between each group were estimated using the Scheff's F test as a post-hoc procedure. The differences were considered to be significant at $P < 0.01$. For the survival fraction, Bartlett test was performed followed by one-way analysis of variance (ANOVA). When the one-way ANOVA was significant, the differences between each group were estimated using the Tukey-Kramer test as a post-hoc procedure. The differences were considered to be significant at $P < 0.05$ or $P < 0.01$.

2.2. Theory

Exposure of cells to US in the presence of NBs generates atomized particles on the surface, indicating the generation of cavitation bubbles [26]. In the medium, NBs and cavitation bubbles interact with each other, and the resulting complex physical forces such as shear stress, liquid jet impact, and shock waves may affect the cell membrane[23][26][37][38][39]. A further investigation of individual physical parameters would lead us into that specialized area of non-spherical bubble dynamics near cell surfaces and

mechanisms of impulsive pressures, and such a digression may shift the focus of our argument. Therefore, we will concentrate on the behavior of a spherical cavitation bubble in an US field and the resulting shock wave phenomenon against the cell.

Cavitation bubble behavior depends on the properties of the surrounding boundaries[40][41]. The critical relative distance affecting the cavitation bubble behavior is defined as L/R_{max}, where L is the distance between the boundary and the bubble inception position and R_{max} is the maximum bubble expansion radius. When NBs are distributed uniformly in the medium and each NB produces a single cavitation bubble at $L/R_{max} > 4$ [42], the bubble motion can be analyzed spherically.

Bubble dynamics

We assume that the US contrast agents are destroyed by US and the internal gas C_3F_8 is trapped in the crevices of the debris of the destroyed agents; additionally, the cavitation bubbles are assumed to be generated from the gas trapped in the crevices. Furthermore, we consider the gas as cavitation nuclei, as modeled by Harvey *et al.* [19]. We assume that spherical cavitation bubbles with a nanometer diameter size can be analyzed as a continuum. The motion of a free spherical cavitation bubble is given by the Keller-Miksis equation [43] as shown below. This equation is corrected to the first order of the Mach number of the bubble wall motion. The error term is the order $\left(\dot{R}/C_L\right)^2$ [44].

$$\ddot{R}\left(1-\frac{1}{C_L}\dot{R}\right)+\frac{3}{2}\dot{R}^2\left(1-\frac{1}{3C_L}\dot{R}\right)=\left(1+\frac{\dot{R}}{C_L}\right)\frac{1}{\rho_L}\left[P_{r=R}(t)-P_C\left(t+\frac{R}{C_L}\right)-P_0\right]+\frac{R}{\rho_L C_L}\frac{dP_{r=R}(t)}{dt} \tag{1}$$

the pressure $P_{r=R}$ at the bubble surface is given by the equation:

$$P_{r=R}(t)=\left(P_0+\frac{2\sigma_L}{R_0}\right)\left(\frac{R_0}{R}\right)^{3r}-\frac{2\sigma_L}{R}-\frac{4\mu_L}{R}\dot{R} \tag{2}$$

the oscillation pressure P_C is given by the equation:

$$P_C(t)=|P_A|\sin\omega t \tag{3}$$

where R is the radius of the bubble; C_L, sound velocity in liquid (1497 m/s); ρ_L, density of water (997 kg/m^3); P_0, atmospheric pressure (101.3 kPa); R_0, the initial bubble radius; γ, adiabatic exponent of a gas (1.07) [45]; μ_L, the liquid shear viscosity (0.89 mPa·s); σ_L, surface tension of water (72 mN/m); P_A, peak positive pressure measured in the experiments; and ω, the circular frequency. Thermal diffusion at the bubble wall and noncondensable gas were ignored.

When a cavitation bubble collapses, a spherical shock wave is emitted as the bubble rebounds. The shock wave interacts with the surrounding cells, resulting in cell membrane damage. The distance of the shock wave propagation from the center of the bubble r_C required to damage to the cell membrane is given by the equation [46]:

$$r_C \approx \frac{P_{max}R_{min}}{\varepsilon_C \rho_L C_L^2} \tag{4}$$

where P_{max} is the maximum pressure when the bubble reaches the minimum radius R_{min} and ε_C is the static critical strain required to damage the membrane. ε_C is estimated to be 0.02–0.03 for the red blood cell membrane [47].

The shock wave pressure Ps, defined as the peak value of the shock wave pressure, decreases as approximately $1/r_S$ while it propagates outward [48]; thus, Ps is given by the equation:

$$P_S = \frac{P_{\max} R_{\min}}{r_S} \tag{5}$$

where r_S is the radial distance of the shock front from the origin.

The acoustic energy Es of a spherical shock wave is given by the equation [49]:

$$E_S = \frac{4\pi r_S^2}{\rho_L C_L} \int_0^{t'} P(t)^2 dt \tag{6}$$

By assuming that the shock wave has wave characteristics that vary in the form of exponential decay with respect to time, we defined the pressure profile P(t) as follows:

$$P(t) \cong P_s \exp\left[\frac{-t \cdot \ln 2}{t_S}\right] \tag{7}$$

where Ps is the peak pressure and t_S is the full width at half-maximum (FWHM) pulse duration of a shock wave (i.e., the time satisfying the condition $(P_S + P_0)/2$), which is numerically obtained. From eqn (6), Es is given as follows [50]:

$$E_S = \frac{2\pi R_{\min}^2 P_{\max}^2 t_s}{\rho_C C_L \ln 2} \tag{8}$$

On the assumption that Es is conserved during the shock wave propagation, t_{rC} at $r = r_C$ is described as follows:

$$t_{r_c} = \frac{\rho_L C_L \ln 2 E_S}{2\pi r_C^2 P_{\max}^2} \tag{9}$$

The shock wave impulse I at $r = r_C$ is given as follows:

$$I_{r_c} = \frac{\rho_L C_L E_S}{2\pi r_C R_{\min} P_{\max}} \tag{10}$$

The equ (1) was calculated up to 50 periodic times using a fourth-order Runge-Kutta method to determine the maximum pressure P_{max}, maximum bubble radius R_{max}, and minimum bubble radius R_{min}, respectively. The chaotic behavior of the bubble motion due to the nonlinear oscillation was not considered.

2.3. Molecular dynamics simulation

Modeling of lipid bilayer

The cell membrane is a thin film (approximately 5 nm) composed of lipids and proteins. The lipid bilayer forms the basic structure of the membrane, while the protein molecules exist as dissolved entities in this layer. Four major phospholipids predominate in the plasma membrane of many mammalian cells: phosphatidylcholine (DPPC), sphingomyelin, phosphatidylserine, and phosphatidylethanolamine [51]. Following the study of Koshiyama

et al. [31], we calculated the interaction of a single lipid bilayer with a shock wave. The lipid bilayer was designed as a 32 DPPC lipid bilayer sandwiched between 2 layers of 2400 water molecules in a rectangular calculation box. The long axis (z axis) of the rectangular box was perpendicular to the bilayer plane (xy plane). The water molecules were calculated using a simple point charge (SPC) model, and all the bond interactions between the atoms in the DPPC molecules were calculated. The stable liquid-crystal phase bilayer was calculated for several tens of nanoseconds under a constant temperature of 50°C and a pressure of 101.3 kPa with periodic boundary conditions.

Shock wave impulse

The shock wave impulse per unit area I is defined as follows [30]:

$$I = \int_0^{t_+} p(t)dt \tag{11}$$

where t is the time; $p(t)$, the pressure near the cells in water; and t_+, the positive phase duration of a half cycle of the shock wave [30]. On the basis of the definition of impulse, the shock impulse I can be regarded as the increment in the momentum of water divided by an area A (the cross-sectional area normal to the z direction of the simulation box) on which the pressure $p(t)$ is exerted. The shock wave impulse is given as follows:

$$I = \frac{M(t_+) - M(0)}{A} \tag{12}$$

where $M(t)$ is the momentum of water at time t. At time $t = 0$, the shock wave did not reach the cells, and the water molecules in the front of the shock wave were at rest; therefore, $M(0) = 0$. When $t = t_+$, the shock wave passed over a small volume of water near the cells, and the momentum $M(t_+) = I \times A$ was transferred to the small volume of water. At the beginning of shock wave simulation, the momentum $M(t_+)$ was applied to water molecules adjacent to the bilayer in a volume $A \times L_Z$, where $A = 3.77$ nm $\times$ 2.72 nm = 10.25 nm^2 and L_Z is the length of the volume of water in the z direction [31]. The choice of L_Z is arbitrary, and we set $L_Z = 4$ nm, which is almost equal to the initial thickness of the bilayer. This is because the present simulation was focused on the behavior of the bilayer with the excess momentum $M(t_+)$ added by the shock wave. The change in the momentum of the water molecules at the beginning of the shock simulation was numerically implemented by the addition of an average velocity V to the thermal velocity of the water molecules in the equilibrated bilayer/water system.

The average velocity V is given by

$$V = \frac{M(t_+)}{mN} = \frac{I \times A}{mN} \tag{13}$$

where m is the weight of a water molecule and N (~1000) is the number of water molecules in the volume $A \times L_Z$. The impulse I is increased from 0 to 100 mPa·s at an interval of 2.5 mPa·s, and V is then changed from 0 to 25600 m/s. The average velocity V corresponds neither to the speed of sound in water nor to the propagation speed of the shock wave. It represents only the increase in the momentum of water molecules due to the shock wave. The modeling of the shock wave by the impulse enables qualitative comparison between the present numerical results and the previous experimental ones.

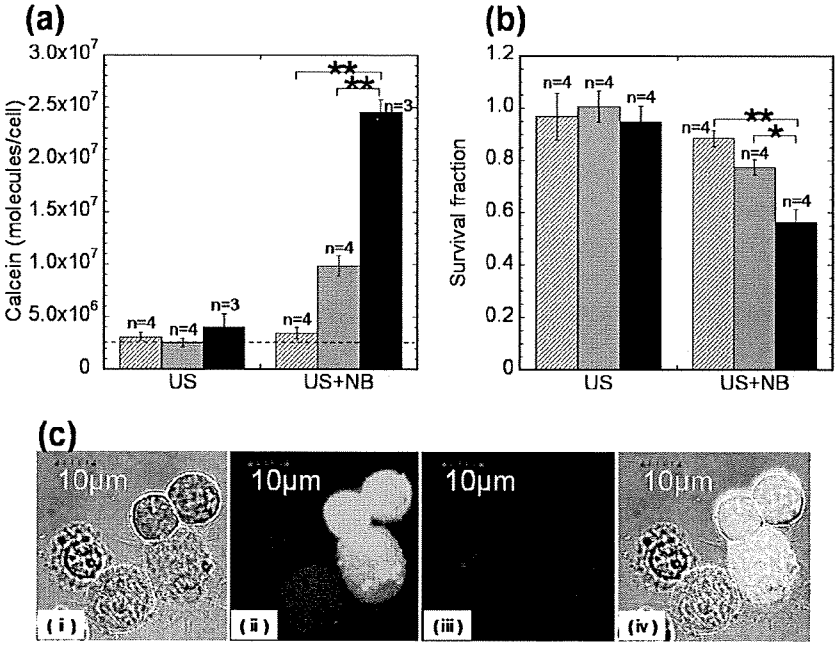

Fig. 3 Effects of NBs on the uptake of calcein (molecular weight: 622). 293T cells with and without NBs were exposed to US with varying US pressure P_A (0.2, 0.3, and 0.5 MPa). Duty ratio, 50%; number of pulses, 2000; pulse repletion frequency (PRF), 250 Hz; and exposure time, 10 s. (a) The number of intracellular molecules per cell. The calcein uptake of the control samples that are without US +NB is indicated as the broken, which is similar to that of US alone. Values are expressed as means ± S.E.M. (n = 3-4), where n is the number of samples. Statistical analysis for the calcein uptake was performed by Kruskal-Wallis test. When the Kruskal-Wallis test was significant, the differences between each group were estimated using the Scheff's F test as a post-hoc procedure. The differences were considered to be significant at $P < 0.01$(**). (b) Survival fractions determined by the MTT assay. Values are expressed as means ± S.E.M. (n = 4). Statistical analysis was performed by Bartlett test followed by one-way analysis of variance (ANOVA). When the one-way ANOVA was significant, the differences between each group were estimated using the Tukey-Kramer test as a post-hoc procedure. The differences were considered to be significant at $P < 0.05$ (*) or $P < 0.01$(**). ▨ : 0.2 MPa, ▩ : 0.3 MPa, ■ : 0.5 MPa. (c) Confocal fluorescence microscopy showing (i) differential interference contrast, (ii) fluorescence images, (iii) representative viable 293T cells exposed to US in the presence of NBs and (iv) color-merged image. In fluorescence staining, PI was used to confirm that the cells showing calcein uptake were viable. Scale bars = 10 μm. US pressure was 0.5 MPa; duty ratio, 50%; number of pulses, 2000; pulse repletion frequency (PRF), 250 Hz; and exposure time, 10 s.

3. Results and Discussion

Observation of cavitation bubbles

First, we investigated the number of calcein molecules delivered into cells in the presence of NBs and US in the experimental system as seen in Fig. 2. The medium containing NBs was a white emulsified suspension. After exposure to US, the medium became transparent, and fragmented debris was found floating on the surface. Atomized particles were detected on the surface with increasing US pressure. In contrast, these particles were not observed with increasing US pressure in the absence of NBs. This phenomenon indicates that impurities in the medium enhance the generation of cavitation bubbles, resulting in the production of capillary waves and subsequent atomized particles [26]. The mean diameter d of the atomized particles due to capillary waves generated by US on the free surface is determined by the liquid surface tension σ_L, liquid density ρ_L, and US frequency f, which is given by eqn (A1). Thus, the mean diameter of the atomized particles is calculated to be 7.9 μm for 1-MHz US. The detailed mechanism of atomized particle generation has been reported by Yule and Al-Suleimani [52].

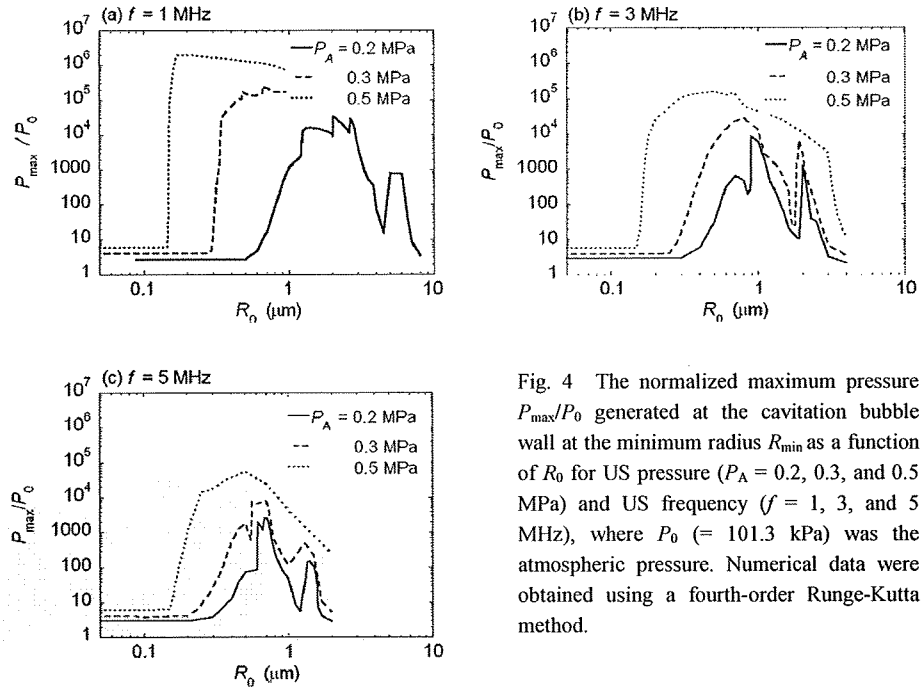

Fig. 4 The normalized maximum pressure P_{max}/P_0 generated at the cavitation bubble wall at the minimum radius R_{min} as a function of R_0 for US pressure (P_A = 0.2, 0.3, and 0.5 MPa) and US frequency (f = 1, 3, and 5 MHz), where P_0 (= 101.3 kPa) was the atmospheric pressure. Numerical data were obtained using a fourth-order Runge-Kutta method.

Uptake of calcein into cells by sonoporation

Figure 3a shows the number of calcein molecules per cell with varying US pressure in the presence/absence of NBs. The duration of exposure to US was 10 s. The calcein uptake of the control samples that are without US +NB is indicated as the broken, which is similar to that of US alone. The presence of the NBs caused a significant increase in the calcein uptake with increasing US pressure, resulting in the delivery of 2.5×10^7 calcein molecules per cell at P_A = 0.5 MPa ($P < 0.01$). The increase in the uptake was associated with the increase in the generation of the atomized particles.

Figure 3b shows the survival fraction of cells exposed to US with and without NBs measured by the MTT assay. US alone did not affect the survival fraction at these pressure values [26]; however, the survival fraction in the presence of NBs decreased with increasing pressure ($P < 0.01$). The uptake of exogenous molecules was inversely proportional to the survival fraction; this finding was in agreement with previous results [26][53]. To confirm that the calcein molecules actually entered the cytoplasm, confocal fluorescence microscopy was performed. Figure 3c shows (i) the differential interference contrast, (ii) fluorescence images, and (iii) representative viable 293T cells exposed to US (0.5 MPa) in the presence of NBs and (iv) color-merged image. In some fluorescence staining, PI was used to confirm that the cells showing calcein uptake were viable and excluded PI (Fig. 3c(iii)). Some cells treated with US in the presence of NB showed intense fluorescence that was uniformly distributed throughout the entire cell.

Motion of cavitation bubbles in the field of ultrasound

From the experimental results, we assumed that cavitation bubbles were related to the transient membrane permeability and subsequent molecular uptake into cells. Next, we analyzed the behavior of a single spherical cavitation bubble in a wide range of parameters including the experimental conditions. Figure 4 shows the relationship between the normalized maximum pressure P_{max}/P_0 generated on the surface of the cavitation bubble wall at the minimum radius R_{min}, and the bubble initial radius R_0, where the atmospheric pressure P_0 was 101.3 kPa. R_0 was varied from 0.05 to 10 μm, US frequency f was 1, 3, and 5 MHz, and the US pressure P_A 0.2, 0.3 and 0.5 MPa. Figure 4a is when f = 1 MHz. The

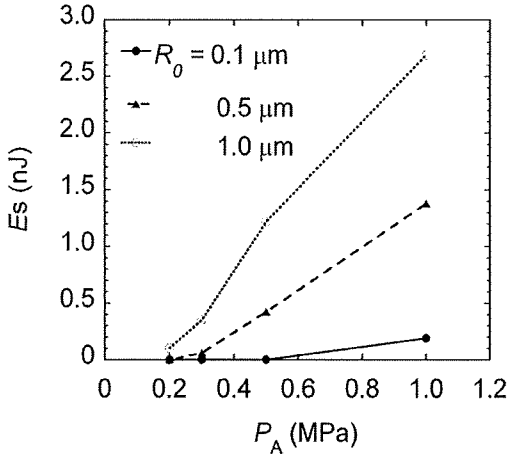

Fig. 5 Relationship between the shock wave energy *Es* given by eqn (8) and the US pressure P_A. The US frequency f was 1 MHz. Numerical data were obtained using a fourth-order Runge-Kutta method.

P_{max}/P_0 increased gradually with increasing R_0, and a peak was obtained at around R_0 = 1.2~3.0 μm. After the first peak, P_{max}/P_0 decreased rapidly, and the second peak was obtained at around R_0 = 5~6 μm. These irregularities are due to the nonlinear cavitation bubble motion. The peak P_{max}/P_0 increased with increasing P_A, and its position shifted to lower values of R_0. When R_0 = 0.635 μm (= 1.27 ÷ 2 μm) that is the initial radius of NBs used in the experiment, P_{max}/P_0 = 4.9 → 1.3 × 10^6 when P_A= 0.2 → 0.5 MPa. In Fig. 3a, the uptake of calcein increases by a factor of 3.6 when P_A= 0.2 → 0.5 MPa. Thus, the increase in P_{max}/P_0 related to the increase in the uptake, indicating that shock waves generated by cavitation bubbles were involved in the uptake of calcein.

Figures 4b and 4c shows the profile of P_{max}/P_0 when f = 3, and 5MHz, respectively. The P_{max}/P_0 decreased when f = 1 → 5 MHz, i.e. the generation of cavitation bubbles is suppressed with increasing US frequency. The fact that the threshold of generation of cavitation bubbles decreases with increasing frequency is in agreement with theoretical [54] and recent experimental results obtained by broadband noise [23]. However, it should be noted that the pressure values were overestimated outside the range of values used for deriving equations.

Interaction of cell membrane with shock wave emitted from a cavitation bubble

When a cavitation bubble reaches its minimum radius R_{min}, it expands and moves the surrounding liquid in the radial direction, thereby resulting in a pressure wave in the vicinity of the bubble wall. The wave propagates outward with a steep pressure front to become a shock wave.

Figure 5 shows the relationship between the shock wave energy *Es* given by eqn (8) and the US pressure P_A at the US frequency f of 1 MHz. The initial bubble radius R_0 varied from 0.1 to 1.0 μm. E_S increased with increasing P_A and R_0, where *Es* was 2.7 nJ at P_A = 1 MPa and R_0 = 1.0 μm.

The shock wave attenuates approximately proportional to $1/r_S$ (r_S: the radial distance of the shock front from the origin) [48][55][56] and interacts with the surrounding cells, resulting in cell membrane damage. In addition, a rapid bubble radial expansion mechanically damages the surrounding cells. Figure 6 shows the shock wave propagation distances (r_C) from the point of its generation as a function of the initial bubble radius R_0 at the US frequency f of 1 MHz, where R_{max} is the calculated maximum bubble radius, and ε_C is necessary to disrupt the membrane. Evans *et al.* [47] reported that ε_C was estimated to be 0.02–0.03 for the red blood cell membrane. In Fig. 6, the shock wave can cause membrane damage at distances less than r_C. The relationship of $r_C > R_{max}$ was satisfied for all values of P_A considered in the present study, i.e., the shock wave was regarded as the main factor of membrane damage rather than bubble expansion. From eqn (A2), the characteristic radius r_0 for a single lipid

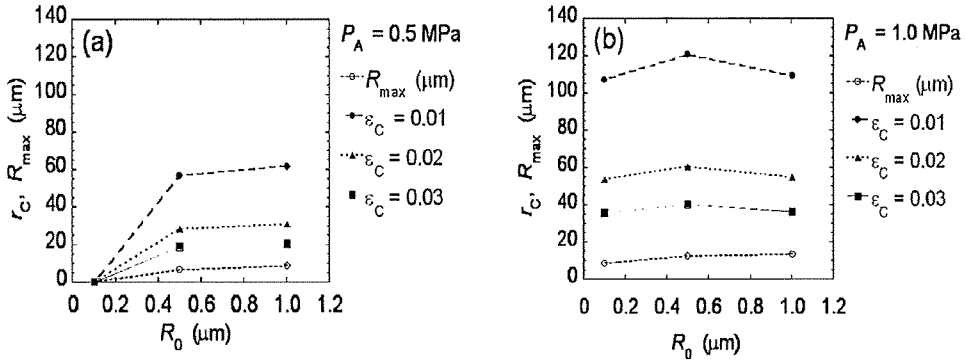

Fig. 6 Potential radius r_C of inducing cell damage by a shock wave from a cavitation bubble and the maximum bubble expansion radius R_{max}, where r_C was given by eqn (4). The initial bubble radius R_0 was 0.1–1.0 μm. The critical strain ε_C was 0.01– 0.03. The US pressure P_A was 0.5–1.0 MPa. The US frequency f was 1 MHz. Numerical data were obtained using a fourth-order Runge-Kutta method.

bubble was calculated to be 19 μm prior to the US exposure. If a single NB produces multiple cavitation bubbles, the conditions $r_C > r_0$ and $r_C > R_{max}$ are satisfied, i.e., the entire area of the medium can be regarded as the shock wave dominant area; therefore, all cells in the medium would be loaded by the shock waves created by the cavitation bubbles.

Figure 7 shows the relationship between P_A and the impulse Ir_c at r_C with varying ε_C, given by eqn (10) at the US frequency f of 1 MHz. When R_0 = 0.5 μm (Fig. 7a), a peak of each characteristic line was obtained at P_A = 0.3 MPa, and the value increased with increasing ε_C. The peak was due to the bubble natural frequency. When R_0 = 1.0 μm (Fig. 7b), peaks were not observed in the figure; however, the lines decreased rapidly with increasing P_A to reach a constant value. This figure indicates that a spherical cavitation bubble with a radius of 0.5–1.0 μm generates impulse values up to 100 mPa·s.

MD simulation of water molecular delivery into the lipid bilayer with shock wave impulse

It is desirable to calculate the number of calcein molecules delivered into cells with MD simulation for comparison with the experimental results. However, to our knowledge, there are no reliable calculation parameters such as force fields or partial charges to reproduce calcein thermodynamic properties and quantum factors. In the present study, we compared the number of water molecules delivered into the lipid bilayer calculated by MD simulation with that of calcein molecules obtained experimentally.

Figure 8 shows the relationship between the shock wave impulse and the penetration rate of water molecules into the bilayer obtained by MD simulation. The penetration ratio of water molecules into the lipid bilayer increased with increasing shock wave impulse. Water molecules were delivered into the cells at the rate of 0–0.3 molecules/(ps·nm^2) at I = 0–11 mPa·s at R_0 = 0.5 μm and ε_C = 0.03 (Figs. 7a and 8). In contrast, at R_0 = 1.0 μm and ε_C = 0.03 (Figs. 7b and 8), water molecules were delivered into the cells at a rate of 0.2–7.6 molecules/(ps·nm^2) at I = 7.2–95 mPa·s.

Although it is reported that water molecules can penetrate into the cytoplasm across the membrane on macroscopic time scales [51], the event rarely occurs on molecular time scales (below nanosecond time scales). However, in the present molecular simulation, water penetration was observed on picosecond time scales. Here, we assumed that at the cell radius r of 5 μm, the shock wave impulse was loaded to a cell from above, and the duration of the impulse was 1 ps. The surface area of the cell hemisphere was given by $2\pi r^2$, and the number of water molecules delivered into the lipid bilayer was calculated to be around 10^7~10^9. The radius of the water molecule was approximately 0.1 nm, and the radius of calcein was estimated to be 0.68 nm [30]. Although the size of the calcein molecule was

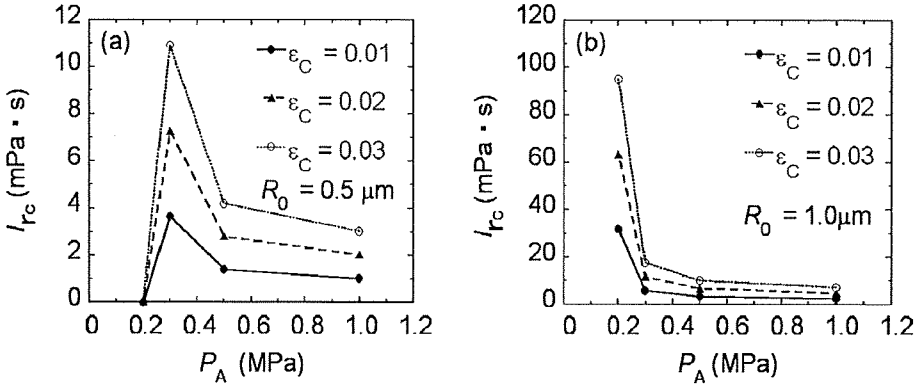

Fig. 7 Relationship between the shock wave impulse I_{rC} (mPa·s) and the US pressure P_A (0.2–1.0 MPa). The US frequency f was 1 MHz. The critical strain ε_C was 0.01–0.03. (a) R_0 = 0.5 μm, (b) R_0 = 1.0 μm. Numerical data were obtained using a fourth-order Runge-Kutta method.

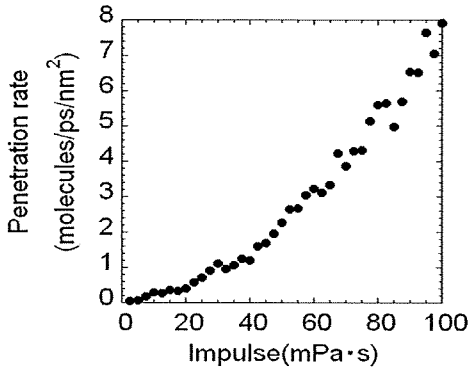

Fig. 8 Relationship between the shock wave impulse and the penetration ratio of water molecules calculated by MD simulation, in which the penetration ratio was calculated in the hydrophobic region at the instant of termination of simulation divided by the cross-sectional area (A = 10.25 nm^2) and the simulation time.

larger than that of the water molecule by a factor of 6.8, the number of delivered calcein molecules in the order of 10^7 per cell (Fig. 3) corresponded to the numerical values. We should note that the estimation of calcein delivery is on experimental time scales (several seconds have elapsed after exposure to ultrasound). On these time scales, the number of delivered water molecules might become considerably larger than that of calcein molecules because many shock waves are generated by pulsating bubbles' impact on membranes. At present, we have investigated water pore formation in lipid bilayers induced by the shock wave impulse [33]. This study suggests that more water penetration induces more larger structural changes in the lipid bilayer. Although it is not possible to estimate the number of water molecules that penetrate into the cells after induction by shock waves by using any other method, the results of the experimental estimation of calcein and numerical estimation of water molecules in the present study imply that the penetration of a large number of water molecules is required before the entry of large molecules. Because water penetration depends on the shock wave impulse generated in the conditions studied here, we believe that the impulse of the shock waves generated by the cavitation bubbles is one of the important parameters for permeabilization during sonoporation.

4. Conclusion

In the present study, experimental, theoretical and numerical analyses were performed to investigate cavitation bubbles mediated molecular delivery during sonoporation. The following conclusions were obtained.

1. Experimental observation using lipid nano/microbubbles indicated that increasing US